https://doi.org/10.1016/j.actbio.2021.08.053


# Nanoparticle-mediated specific elimination of soft cancer stem cells by targeting low cell stiffness

Xi Chen[1,2], Yadi Fan[2], Jinghua Sun[2], Zhipeng Zhang[2], Ying Xin[1,2], Keming Li[1,2], Kai Tang[1,2], Pengyu Du[1,2], Yiyao Liu[3], Guixue Wang[4], Mo Yang[2]*, Youhua Tan[1,2]*

[1]The Hong Kong Polytechnic University Shenzhen Research Institute, Shenzhen 518053, Guangdong, China

[2]Department of Biomedical Engineering, The Hong Kong Polytechnic University, Hong Kong SAR, China

[3]Department of Biophysics, School of Life Science and Technology, University of Electronic Science and Technology of China, Chengdu 610054, Sichuan, China

[4]Key Laboratory for Biorheological Science and Technology of Ministry of Education, State and Local Joint Engineering Laboratory for Vascular Implants, Bioengineering College of Chongqing University, Chongqing, 400030, China.

*Corresponding author

Email: mo.yang@polyu.edu.hk; phone: 852-2766-4946; fax: 852-2334-2429

Email: youhua.tan@polyu.edu.hk; phone: 852-3400-8897; fax: 852-2334-2429

Postal address: ST406, Department of Biomedical Engineering, The Hong Kong Polytechnic University, Hong Kong SAR, China

Keywords: cellular stiffness, cancer stem cell, cellular uptake, mechanomedicine, nanoparticle

**Abstract:** As the driving force of tumor progression, cancer stem cells (CSCs) hold much lower cellular stiffness than bulk tumor cells across many cancer types. However, it remains unclear whether low cell stiffness can be harnessed in nanoparticle-based therapeutics for CSC targeting. We report that breast CSCs exhibit much lower stiffness but considerably higher uptake of nitrogen-doped graphene quantum dots (N-GQDs) than bulk tumor cells. Softening/stiffening cells enhances/suppresses nanoparticle uptake through activating/inhibiting clathrin- and caveolae-mediated endocytosis, suggesting that low cell stiffness mediates the elevated uptake in soft CSCs that may lead to the specific elimination. Further, soft CSCs enhance drug release, cellular retention, and nuclear accumulation of drug-loaded N-GQDs by reducing intracellular pH and exocytosis. Remarkably, drug-loaded N-GQDs specifically eliminate soft CSCs both *in vitro* and *in vivo*, inhibit tumor but not animal growth, and reduce the tumorigenicity of xenograft cells. Our findings unveil a new mechanism by which low cellular stiffness can be harnessed in nanoparticle-based strategies for specific CSC elimination, opening a new paradigm of cancer mechanomedicine.

**Statement of significance**:

Low cell stiffness is associated with high malignancy of tumor cells and thus serves as a mechanical hallmark of CSCs. However, it remains unclear whether cellular stiffness can be exploited for specific targeting of soft CSCs. This work reports that soft CSCs exhibit high N-GQD uptake compared to stiff tumor cells, which is regulated by cellular stiffness. Further, soft CSCs have enhanced drug release, cellular retention, and nuclear accumulation of drug-loaded N-GQDs, which enable the specific elimination of malignant CSCs both *in vitro* and *in vivo* with minimal side effect. In summary, our study demonstrates that CSC's low stiffness can be harnessed as a mechanical target for specific eradication, which provides a new paradigm of cancer mechanomedicine.

## 1. Introduction

Cancer stem cells (CSCs) have been proposed to reside at the apex of tumor cell hierarchy with high tumorigenic and metastatic potential [1]. These malignant cells exhibit considerable resistance to conventional chemo-/radio-therapy, which is believed to underlie the failure of current cancer therapeutics and the incidence of cancer relapse [2]. Therefore, CSCs hold the essential traits to drive tumor progression, drug resistance, and cancer recurrence and hence become the major target in cancer therapeutics. However, the unique traits of CSCs have posed grand challenges to their elimination for effective cancer treatment. It is thus necessary to devise novel strategies for specific CSC targeting.

Nanoparticles have shown great promise in cancer therapy as the carrier of therapeutic drugs [3]. Various surface proteins have been identified as functional CSC markers, including CD133, CD44, CD20, CD90, CD15, and aldehyde dehydrogenase [1]. These markers have been exploited to functionalize the nanoparticle surface, which can facilitate the delivery of therapeutic drugs specifically into CSCs via the interaction between the ligands on the nanoparticle surface and the receptors on the CSC membrane for chemotherapy and thermotherapy. For example, lipoprotein-mimetic nanoparticles coated with CD15 antibody can penetrate the blood–brain barrier and deliver the sonic hedgehog inhibitor effectively to brain CSCs in medulloblastoma [4]. Magnetic nanoparticles with the encapsulation of chemotherapy drug and the coating of CD20 antibody can be efficiently internalized by lung CSCs to induce substantial cell apoptosis under an alternating magnetic field due to the combined effect of chemotherapy and thermotherapy [5]. However, these surface proteins are dynamically evolving and thus may not be able to faithfully label CSCs during tumor progression. Many studies have casted doubt on the reliability of these proteins as functional CSC markers and thus the efficacy of surface marker-based nanoparticle-mediated cancer

therapy [6,7]. Therefore, it is essential to harness reliable features as faithful CSC markers, which will facilitate the development of novel nanoparticle-based strategies for specific CSC elimination.

To improve the efficacy of nanoparticle-based drug delivery in cancer therapy, considerable advances have been achieved to enhance cellular uptake of nanoparticles by optimizing their physical dimension and surface chemistry, which can facilitate the targeting of bulk tumor cells but not CSCs [8–12]. It has become increasingly clear that mechanical cues play important roles in regulating cellular functions and tumor progression [13,14], including mechanical properties of cancer cells [15]. Cell mechanics are inversely correlated with tumor malignancy in many types of cancer: primary cancer cells derived from cancer patients exhibit less F-actin assembly and lower cellular stiffness than their healthy counterparts [16]; highly metastatic tumor cells are much softer than weakly metastatic cells [17]. Importantly, malignant CSCs hold considerably lower level of stiffness than bulk tumor cells [18–20]. Recent evidence shows that soft tumor cells isolated by microfluidic sorting exhibit much higher stemness and tumorigenicity than stiff ones [21]. In addition to the correlation between cell stiffness and tumor malignancy, cell mechanics critically influence various cellular functions, including adhesion, proliferation, stemness, and motility [22,23]. Low stiffness protects CSCs from T cell-mediated cytotoxicity and confers the advantage of tumor immune evasion [24]. The reduced cellular stiffness enhances the survival of circulating tumor cells and CSCs in fluid shear flow and facilitates extravasation during hematogenous dissemination [25,26]. Further, cancer cell cytoskeleton plays important roles in nanoparticle internalization [27]. Therefore, low cellular stiffness is not only a unique feature of CSCs across many types of cancer but also an important regulator of tumor cell functions.

However, the roles of cell mechanics in cellular uptake and nanoparticle-based elimination of soft CSCs remain unknown.

Nanoparticles enter living cells through various mechanisms, in which one important internalization manner is endocytosis [3]. During the process of cellular uptake, nanoparticles first interact with the components of the cell membrane to initiate endocytosis and are then wrapped by the cell membrane, which can pinch off to form endocytic vesicles. The physicochemical properties of nanoparticles, such as shape, surface charge, and size, play important roles in their interaction with the cell membrane during the endocytosis process. First, it is easier for living cells to internalize nanoparticles with spherical than anisotropic shape, since it takes longer time for the cell membrane to wrap nanoparticles with irregular shape [28,29]. Second, positively charged nanoparticles have a stronger temporary disruptive effect on the lipid bilayer of the cell membrane, which facilitates the internalization process [3]. Third, the main endocytosis mechanisms, including clathrin/caveolae-dependent endocytosis, are based on the inward budding of plasma membrane proteins. It is challenging for the cell membrane to completely wrap large-sized nanoparticles, which impedes efficient endocytosis [30]. Therefore, nanoparticles with spherical shape, small size and positive surface charge, as well as good fluorescence for intracellular tracking can be a good model to study mechanotargeting of CSCs.

As a new generation of fluorescence nanoparticles, graphene quantum dots (GQDs) have been widely used as bioimaging agents and drug delivery carriers due to the promising fluorescence property, small size, spherical shape, tailored surface charge by element doping, high biocompatibility, and high surface-to-volume ratio for drug loading [31,32]. This study adopted fluorescent nitrogen-doped GQDs (N-GQDs) as chemotherapy drug nanocarrier and explored the role of cell mechanics in nanoparticle uptake. Mechanistically, the effect of cell

stiffness on the endocytosis pathways was examined. Further, drug release, nuclear localization, and cellular retention of doxorubicin-conjugated N-GQDs (N-GQD@Dox) were compared between soft CSCs and stiff bulk tumor cells. Finally, the efficacy of N-GQD@Dox for specific targeting of soft CSCs and cancer therapy was demonstrated in both *in vitro* breast CSC model and *in vivo* xenograft model. Compared with free drugs, N-GQD@Dox inhibited tumor but not animal growth, and specifically eliminated breast CSCs *in vivo*, thereby reducing the tumorigenicity of xenograft cells and potentially suppressing tumor recurrence.

## 2. Materials and methods

### 2.1 Synthesis of nitrogen-doped graphene quantum dots

Nitrogen-doped graphene quantum dots (N-GQDs) were prepared by a bottom-up hydrothermal method. Briefly, 0.105 g of citric acid monohydrate (CA·H2O) and 1 ml of Ethylenediamine (EDA) were dispersed in 4 ml of distilled (DI) water under vigorous stirring. The mixture was then added to a 10 ml Teflon-lined autoclave and heated at 200 °C for 4 h. A yellow solution was obtained after cooling down to room temperature. After centrifugation, the supernatant was retrieved and passed through a 0.22 μm microporous filter membrane to further remove the residual large particles. The product was then purified by dialysis against DI water for 8 h (MWCO=1000) to remove excess reactants. Finally, the obtained light yellow N-GQD aqueous dispersion was lyophilized for further characterization.

### 2.2 Characterization of N-GQD and N-GQD@Dox complex

The shape, size and morphology of the synthesized N-GQDs and N-GQDs@Dox were characterized with a JEOL-2100F transmission electron microscopy (TEM) equipped with an

Oxford Instrument energy-dispersive X-ray (EDX) spectrometry system. Fourier transform infrared spectrum (FTIR) was analyzed using a PerkinElmer Spectrum 100 FT-IR spectrometer (PerkinElmer Inc., USA). UV–Vis spectra were performed on a UV/Visible spectrophotometer (Biochrom., England). The excitation and emission spectra were measured by a FLS920P Edinburgh Analytical Instrument (Edinburgh Instruments, England).

### 2.3 Drug loading capacity of N-GQD

The loading of Dox molecules onto N-GQD was determined by measuring absorption at 484 nm using a UV–visible spectrophotometer (Ultrospec 2100 Pro., GE). Generally, N-GQDs (1 mg) were stirred and mixed with Dox (1mg) in 1 ml of DI water for 48 h. The large precipitate was removed by centrifugation and the mixture was then purified with 3 kDa ultrafiltration to obtain N-GQDs@Dox complex. The unbound Dox was quantified via analyzing the absorbance of the supernatant at the characteristic 484 nm. The drug loading capacity Q was defined as the following equation:

$$Q = \frac{(C_0 - C_1) * V}{m}$$

where $C_0$ was the initial concentration of drug molecule and $C_1$ was the concentration of unbound drug molecule after adsorption. $C_0$ and $C_1$ were calculated from the calibrated relationship between Dox concentration and the absorption spectra at 484 nm. $V$ was the volume of Dox solution and $m$ was the mass of the sorbent.

### 2.4 The measurement of Dox release from N-GQD@Dox

The Dox release was measured following the dialysis method. The prepared N-GQD@Dox solution was sealed into a dialysis tube with a membrane (1 kDa cut-off) in cap and immersed into PBS at pH 5.5 and 7.0, respectively. The whole setup was then placed in a

shaker at the speed of 60 rpm. The PBS was collected at the indicated time points and the amount of released Dox was measured by UV-Vis spectrophotometer at 484 nm.

### 2.5 Breast cancer cells and culture

Human breast cancer cell line MCF-7, MDA-MB-231, and SKBR3 cells (ATCC) were cultured in Dulbecco's Modified Eagle Medium (DMEM, HyClone, Logan, UT) with 10% fetal bovine serum (HyClone) and 1% penicillin/streptomycin (HyClone) at 37°C and 5% $CO_2$. Normal breast epithelial MCF-10A cells (ATCC) were cultured in DMEM/F12 (Invitrogen#11330-032) with 5% horse serum (Invitrogen#16050-122), EGF (20 ng/ml), hydrocortisone (0.5 mg/ml), cholera toxin (100 ng/ml), insulin (10 μg/ml), and 1% penicillin/streptomycin (HyClone). Cells were passaged every 3-4 days with 0.25% Trypsin (HyClone).

### 2.6 Cell treatment with pharmacologic drugs, plasmids, and siRNAs

Cells were treated with 10 μM Y-27632 (Selleckchem), 6 μM blebbistatin (Selleckchem), 20 nM Jasplakinolide (Tocris #2792/100U), or 1 nM Narciclasine (MedChemExpress #HY-16563) for 12 h for the modulation of cell mechanics. To inhibit nanoparticle endocytosis, 25 μM Genistein (Selleckchem #S1342), 3 μM Chorpromazine (Selleckchem #S5749), or both were used to treat cells for 30 min. Breast cancer cells were transfected with constitutive active (CA)-MLCK, CA-ROCK, and empty plasmids (control) by lipofectamine 3000 Reagent (Thermo Fisher). 50 ng/ml doxycycline (TargetMol) was used to active the plasmids in the transfected cells for two days. siRNAs (100 nM) were employed to knock down mDia1 and MLCK by the transfection of lipofectamine 3000 Reagent (Thermo Fisher) for 48 h.

### 2.7 The preparation of polyacrylamide gels

Polyacrylamide gels were prepared following the protocol reported elsewhere [33]. The 8-kPa gel rigidity was determined by the concentrations of bis-acrylamide crosslinker (2%) and acrylamide (40%) (Bio-Rad). The gel surface was activated by the crosslinker Sulfo-SANPAH (sulfosuccinimidyl 6-(4′-azido-2′-nitrophenylamino) hexanoate) (Pierce) and then coated with collagen (200 μg/ml) or fibronectin (20 μg/ml) before plating cells.

**2.8 Confocal imaging of N-GQD intensity and quantification**

Cells were cultured on 8-kPa PA gels overnight and N-GQDs were added at the concentration of 80 μg/ml or others as specified and further cultured for 4 h at 37°C. Before imaging, the cells were gently washed by PBS for 2 times to remove the non-endocytosed nanoparticles. These cells were then mounted at the stage of Leica TCS SPE confocal microscope for imaging. The wavelength of the excitation light was 405 nm for N-GQD and 488 nm for Dox and N-GQDs@Dox. The wavelength of the emission light was 430-500 nm for N-GQD and 530-730 nm for Dox and N-GQDs@Dox, respectively. Bright field images of the cells were also captured. The fluorescence intensity of N-GQDs or Dox and cell area were analyzed by ImageJ, from which the fluorescence intensity per unit area could be calculated. For each condition, at least 60 cells were imaged. For 3D confocal imaging, cell membrane and nuclear were labeled by CellTrackerTM Deep Red Dye (Thermo Fisher C34565) and Hoechst 33342 solution (Thermo Fisher 62249), respectively. The images were taken every 0.5 μm in the direction of cell thickness by confocal imaging and the reconstruction of 3D cell shape was conducted using the Imaris 3/4D Analysis software (Oxford Instruments).

**2.9 Immunofluorescence staining**

Cells were plated on gelatin-coated coverslips in 24-well-plate overnight and then fixed with 4% formaldehyde (Sigma Aldrich) for 30 min at room temperature. The fixed coverslips were washed 3 times by PBS for 15 min and then incubated with 0.1% Triton X-100 (SAFC) in 1% BSA for 1 h at room temperature for permeabilization. After washing the cells with PBS, 1x green fluorescent phalloidin conjugate working solution (AbCam) was added to the cells for 1 h for F-actin staining. To stain Bmi-1, CXCR4, clathrin, and caveolin-1, the cells were incubated with the corresponding primary antibody in 1% BSA overnight at 4°C. The coverslips were then washed with PBS and incubated with goat anti-rabbit IgG H&L (Alexa Fluor® 488) (Abcam), goat anti-mouse IgG (H+L) highly cross-adsorbed secondary antibody, and Alexa Fluor Plus 488 (Invitrogen) in 1% BSA for 1 h at room temperature, respectively. After gentle washing, the cells were counterstained with DAPI (Thermo Fisher) for nuclear staining. For each condition, at least 100 cells were imaged using the inverted fluorescent microscope (Nikon) and the fluorescence intensity was analyzed by ImageJ.

**2.10 Atomic force microscopy for cell stiffness measurement**

Atomic force microscope (AFM, Bruker Catalyst) was used to measure cell stiffness. Cells were cultured in 68-mm petri dishes overnight and silicon nitride cantilevers with the spring constant k of 0.02-0.08 N/m at room temperature were chosen. The force F between tip and cell was the product of the cantilever deflection δ and k, i.e., $F = k \times \delta$. The force (F) between the measured cell and the cantilever's tip was the product of the cantilever deflection δ and k, i.e., $F= k \times \delta$. The cell Young's modulus E could be calculated by fitting the force-indentation curves with Hertzian model for a pyramidal tip, i.e., $F=2/\pi\times\tan(\alpha)\times E/(1-\nu^2)\times d^2$, where α is the half tip angle, $\nu$ is 0.5, and d is the indentation depth. d was kept within 500 nm at 1 Hz to avoid potential substrate effects and cell damage.

**2.11 3D soft fibrin gels for CSC selection**

3D soft fibrin gel (1 mg/ml) was used to select tumorigenic cancer stem cells [18,34]. In brief, single cells were detached by trypsin and suspended in culture medium with cell density at $6x10^5$/ml. Fibrinogen (SEA-133) was diluted to 2 mg/ml by T7 buffer (50 nM Tris, 150 nM NaCl, pH7.4). Diluted fibrinogen and cell solution were then mixed equally. 5 µl of thrombin (SEA-135) with the concentration of 100 U/ml was pre-added to each well in the 24-well-plate. The mixture of cell and fibrinogen was then added and mixed gently with thrombin. The plate was placed in the cell culture incubator at 37°C for 15 min. After the gel was solidified, 1 ml of cell culture medium was added into each well. CSCs could be retrieved from the soft gels after 7-day culture.

**2.12 Quantitative RT-PCR**

Aurum Total RNA Mini Kit (Bio-Rad) was used to extract the total mRNA. The complementary DNA was synthesized by RevertAid First Strand cDNA Synthesis Kit (Thermo) according to the supplier's protocol. Forget-Me-Not EvaGreen qPCR Master Mix with Rox (Biotium) and CFX96 Real-Time System (Bio-Rad) were used for quantitative RT-PCR analysis. All the primer sequences were listed in the Supplementary Table 1. The expressions of all genes were normalized against human glyceraldehyde 3-phosphate dehydrogenase (GAPDH).

**2.13 Western Blot**

Proteins were extracted from the lysed cells by Men-PerTM Plus membrane protein extraction kit (Thermo Fisher #89842). Trans-Blot Turbo (Bio-Rad) was used to transfer proteins from 8% sodium dodecyl sulfate polyacrylamide gel electrophoresis gel (SDS-PAGE) to a PVDF western blot membrane. The transferred membrane was incubated with 3% BSA and then the primary antibodies of clathrin and caveolin-1 (AbCam) at 4°C

overnight and with secondary antibodies, goat anti-mouse IgG (H+L)-HRP conjugate and goat anti-rabbit IgG (H+L)-hRP Conjugate (Bio-Rad) for 2 h. GAPDH (AbCam) was used for reference. The membranes were then incubated with ClarityTM and Clarity MaxTM Western ECL Blotting Substrates and images were captured using ChemiDocTM Imaging System (Bio-Rad).

**2.14 Soft agar colony formation assay**

Soft agar assay was used for the measurement of colony formation ability. Briefly, 3% of agarose (Sigma #A4018) was autoclaved and diluted to 1% using DMEM. 2 ml of the agarose solution was added to each well of the 6-well-plate and allowed to cool down for 30 min at room temperature. Cells were then mixed with 3% of agarose, DMEM, and FBS at appropriate ratios to achieve 0.4% agarose and 10% FBS. Each well contained 5000 cells. The gels were then allowed to cool down at room temperature for 30 min. 300 µl of cell culture medium was added to each well every 5-6 days. The cells were cultured in soft agar up to 28 days and then stained with 0.005% Crystal Violet for 1 h in darkness. The colony number of each well was counted under microscope.

**2.15 Animal experiment**

The Guide for the Care and Use of Laboratory Animals of the National Institutes of Health was strictly followed in all animal experiments. The experimental protocol was approved by the Animal Subjects Ethics Sub-Committee (ASESC) of the Hong Kong Polytechnic University. Every effort was made to minimize the pain and suffering of animals.

For the 1$^{st}$ generation of tumor xenografts, female BALB-nude mice (5-week old) were used for the animal experiment and treated with β-estradiol (ApexBio) two days before tumor cell injection. $5\times10^6$ of MCF-7 cells were mixed with the same volume of matrigel solution

(Corning® Matrigel® Matrix Phenol Red-free, #356237) and then subcutaneously injected into the right hind flanks of mice. The tumors were allowed to grow for 7 days to reach the volume of around 100 $\mu m^3$. The mice were then randomly grouped into 4 groups, i.e., Control, Dox, N-GQD, and N-GQD@Dox, and there were at least 6 mice for each group. PBS, Dox (5 mg/kg), N-GQD (5 mg/ml), and N-GQD@Dox (5 mg/kg) was intraperitoneally injected into the mice every 4 days up to 28 days. Tumor size and animal body weight were measured every 4 days and the tumor volume was calculated as Volume=1/2×width×length$^2$. All mice were euthanized at the end of the experiment and tumor tissues were retrieved and weighed. The xenografts were then cut into small pieces and dissolved by collagenase solution. Single cells were obtained for further experiments. For the 2$^{nd}$ generation of tumor xenografts, $5\times10^6$ of tumor cells derived from the 1$^{st}$ generation of tumor xenografts in each group (i.e., Control, Dox, N-GQD, and N-GQD@Dox) together with the same volume of matrigel solution were subcutaneously injected into the right hind flanks of nude mice. The size of the generated tumors was measured at day 45 after injection.

**2.16 MTS for cell viability measurement**

Cell viability was detected by MTS assay. 100 μl of cell solution with the density of $5x10^4$/ml was plated into each well of the 96-well plate overnight. After removing the medium, 20 μl of sterilized CellTiter 96 Aqueous One Solution (5mg/ml, Promega) was added to each well. After 4 h incubation in darkness at 37°C, the absorbance of each well was measured at 490 nm by the Benchmark Plus microplate reader (Bio-Rad). The experiment was carried out 3 times with at least 3 wells for each condition.

**2.17 Intracellular pH measurement**

The intracellular pH of cancer cells was measured following the manufacturer's protocol (Thermo Fisher). The curve of the pH and the fluorescence intensity of the indicator was calibrated using the Intracellular pH Calibration Buffer Kit (Thermo Fisher #35379). In brief, cells were plated on 8-kPa polyacrylamide gel overnight and then incubated with pHrodo$^{TM}$ Green AM Intracellular pH Indicator (Thermo Fisher #35373) for 30 min. To determine the calibration curve, three groups of cells were incubated in the Intracellular pH Calibration Buffer with 10 μM Valinomycin and 10 μM Nigericin at pH5.5, 6.5, and 7.5 for 5 min, respectively. The fluorescence intensity of the indicator was measured under the Leica TCS SPE confocal microscope. The intensity was analyzed by ImageJ and the relationship between the intracellular pH and the fluorescence intensity of the indicator was established by fitting the data linearly. The cells after various treatments were then treated similarly as described above and the fluorescence intensity of the indicator was measured. The intracellular pH was obtained from the calibrated pH-fluorescence curve.

**2.18 Flow cytometry measurement**

For each condition, cells were detached by 0.2% EDTA and incubated with CD133 antibody (BioLegend #301706) diluted by 2% FBS in PBS at 4°C for 30 min. The percentage of CD133+ subpopulation in each condition was then detected by BD Accuri C6 flow cytometer (BD Biosciences, USA).

**2.19 Data analysis**

All the results were represented by mean ± standard error of the mean (SEM). The statistics between two conditions and among three or more conditions were analyzed by two-tailed Student's t-test and analysis of variance (ANOVA), respectively. The post hoc Tukey or

Bonferroni test was adopted in the ANOVA analysis for the comparisons with equal or unequal sample sizes. *, $p<0.05$; **, $p<0.01$; ***, $p<0.001$.

## 3. Results and discussion

### *3.1 Synthesis of N-GQD@Dox nanocomplex for specific CSC targeting*

N-GQDs were synthesized using a hydrothermal approach and monodispersed with an average size of ~2.7 nm measured by TEM (Fig. 1A) [32]. The X-ray photoelectron spectroscopy analysis shows that N-GQD was composed of C, N, and O elements (Fig. 1B-D). The Fourier-transform infrared spectroscopy analysis shows the peaks at 1335 $cm^{-1}$ and 1012 $cm^{-1}$, indicating the presence of CN and CO oxygen-containing groups, respectively (Fig. 1E). N-GQDs emitted a strong fluorescence signal at ~460 nm under the excitation of 360 nm that was independent of the excitation wavelength (Fig. 1F). After loading doxorubicin (Dox) to N-GQDs, the complex showed two peaks at 346 nm and 484 nm (Fig. 1G), indicating the formation of N-GQDs@Dox. The conjugation of Dox to N-GQDs slightly increased the nanoparticle size from 2.7 nm to 3.3 nm measured by TEM (Fig. 1A) and from 30.5 nm to 32.5 nm measured by nanoparticle tracking analyzer (Fig. S1A). It is known that nanoparticle tracking analysis measures the hydrodynamic size of nanoparticles, which is larger than the size measured by TEM [35]. N-GQDs and N-GQD@Dox exhibited similar positive Zeta potential (around +16 mV) (Fig. S1B). Further, N-GQD and Dox served as donor and acceptor in N-GQD@Dox according to the principle of fluorescence resonance energy transfer (FRET) (Fig. 1H). The emitted light of N-GQD was transferred to the attached Dox molecules, which was attenuated when Dox was released from N-GQD surface (Fig. 1I). By monitoring the ratiometric FRET signal change of two emission channels, the

drug release process can be determined. The cumulative Dox release profiles of N-GQD@Dox show that the drug release rate at pH 5.5 was ~2 times of that at pH 7.0 (Fig. 1J), suggesting the dependence of drug release on the pH. Further, the cytotoxicity assay shows that cell viability was higher than 95% even at high concentrations of N-GQDs (Fig. 1K), suggesting the excellent biocompatibility. In summary, the small size, excitation-independent emission, low cytotoxicity, positive surface charge, and pH-dependent drug release make N-GQD an excellent carrier for drug delivery.

### *3.2 Nanoparticle uptake is inversely associated with tumor cell stiffness*

We next explored the relationship between cellular uptake and cell stiffness. Breast cancer and normal cells were co-cultured with N-GQDs on 8-kPa polyacrylamide (PA) gels coated with collagen that mimicked the mechanical microenvironment of breast tumors [36]. Confocal imaging shows that N-GQDs were internalized into the cell body instead of stuck to the cell membrane (Fig. S2A, Movie S1). The fluorescence intensity of N-GQDs per unit cell area was used to represent cellular uptake. Nanoparticle uptake was saturated after co-culturing tumor cells with N-GQDs for 4 h (Fig. S2B-D), which was adopted in this study. We found that breast cancer cells exhibited less F-actin assembly and lower stiffness but much higher uptake of N-GQDs than normal breast cells (Fig. 2A-D, Fig. S2E-F). Further, breast CSCs selected by 3D soft fibrin exhibited higher stemness (Fig. S3) [18,34] and lower levels of F-actin assembly and mechanical stiffness but took up more N-GQDs than bulk tumor cells on collagen-coated 8-kPa PA gels (Fig. 2E-F), suggesting that soft cancer cells have enhanced cellular uptake. To test the possibility that the enhanced nanoparticle uptake in soft CSCs depends on specific ligand, breast cancer cells and CSCs were further cultured on fibronectin-coated 8-kPa PA gels. We found that nanoparticle uptake was still higher in soft CSCs than stiff bulk tumor cells (Fig. S4A-B), suggesting that the finding of high

cellular uptake in soft CSCs is not ligand-dependent. The concentrations of both serum and nanoparticle influenced N-GQD internalization, while soft CSCs always had higher cellular uptake than bulk tumor cells under the same condition (Fig. S4C-F). All these results suggest that cellular uptake of nanoparticles is inversely associated with cellular stiffness.

### *3.3 Softening/stiffening tumor cells enhances/suppresses cellular uptake*

We further explored the influence of cellular stiffness on nanoparticle uptake. Pharmacologic treatment of breast cancer cells by Blebbistatin (myosin II inhibitor) or Y-27632 (Rho-associated coiled-coil containing kinases or ROCK inhibitor) significantly reduced F-actin assembly (Fig. 3A, Fig. S5A and F) and cellular stiffness (Fig. S6A, Fig. S4G). Importantly, softening cells considerably enhanced cellular uptake of N-GQDs to the similar level of soft CSCs (Fig. 3B, Fig. S5H, J, and K), which was not due to the increased cell apoptosis (Fig. S5E and I). Note that moderately softening bulk tumor cells by 2 and 6 μM Blebbistatin progressively increased nanoparticle uptake, while considerably softening them by 20 μM Blebbistatin reduced cellular uptake (Fig. S6E). Similarly, softening CSCs enhanced N-GQD uptake in the presence of 2 μM Blebbistatin, while exhibited no or even suppressive effect with 6 and 20 μM Blebbistatin, respectively (Fig. S5L, Fig. S6F). Silencing myosin light chain kinase (MLCK) or mDia1 significantly reduced F-actin assembly (Fig. 3C, Fig. S5B) and cell stiffness (Fig. S6B) but considerably increased nanoparticle uptake (Fig. 3D). These findings suggest that softening cancer cells increases cellular uptake. Further, pharmacologic treatment by Jasplakinolide (F-actin stabilizer) or Narciclasine (Rho signaling activator) significantly increased F-actin assembly (Fig. 3E, Fig. S5C, M) and cellular stiffness (Fig. S5N, Fig. S6C). Importantly, stiffening cells considerably suppressed cellular uptake of fluorescent N-GQDs (Fig. 3F, Fig. S5M, O). Further, overexpressing constitutive active (CA) form of MLCK or ROCK significantly enhanced F-actin assembly (Fig. S5D, P, and T) and

cellular stiffness (Fig. S6D). Stiffening bulk tumor cells significantly suppressed the internalization of N-GQDs (Fig. 3G, H, Fig. S5P, Q). Similarly, stiffening breast CSCs substantially reduced cellular uptake, while concurrently softening these cells rescued this inhibitory effect in both bulk tumor cells and CSCs (Fig. 3G-I; Fig. S5R, S). The altered uptake was not due to the treatment effect on cell apoptosis (Fig. S5E, I, and T). These results indicate that stiffening cancer cells suppresses nanoparticle uptake. In summary, all these findings suggest that cell mechanics regulate cellular uptake of nanoparticles.

### *3.4 Cell mechanics regulate cellular uptake partially via clathrin-/caveolae-mediated endocytosis*

We next set to unveil the mechanisms underlying cell mechanics-dependent nanoparticle uptake. Since nanoparticles enter living cells through various mechanisms, including clathrin- and caveolae-dependent and/or independent endocytosis [3], the protein expressions of clathrin and caveolin-1 were thus compared between soft and stiff cancer cells. Softening cells enhanced the expressions of clathrin and caveolin-1 proteins (Fig. 4A-C, Fig. S7A-C), while stiffening cells suppressed their expressions, which were supported by immunoblotting (Fig. 4D and E). Further, soft CSCs expressed higher levels of clathrin and caveolin-1 proteins than stiff bulk tumor cells (Fig. 4F-G, Fig. S7D-E). These results suggest that cell mechanics influence clathrin- and caveolae-mediated endocytosis pathways. To explore whether cell mechanics regulate nanoparticle uptake through endocytosis, the intracellular locations of nanoparticles, clathrin, and caveolin-1 were examined. Softening cancer cells increased the colocalization between N-GQDs and clathrin/caveolin-1 to the levels of CSCs, while stiffening cells reduced the colocalization (Fig. S8). Further, breast cancer cells were treated with Genistein and Chlopromazine, which inhibits caveolae- and clathrin-mediated endocytosis, respectively. Inhibiting these endocytosis pathways suppressed nanoparticle

uptake (Fig. S7F-G). Importantly, softening cells enhanced cellular uptake, while concurrently silencing caveolae- or clathrin-dependent endocytosis reduced nanoparticle uptake to the similar level of control group (Fig. 4H-I, Fig. S7H-I). Further, silencing either endocytosis pathway reduced cellular uptake of breast CSCs to the similar level of bulk tumor cells (Fig. 4J, Fig. S7J). The alteration in cellular uptake after the inhibition of the endocytosis pathways was not due to the effect of pharmacologic treatment on cell viability (Fig. S9). All these results suggest that cell mechanics regulate cellular uptake partially via the effects on caveolae- and clathrin-dependent endocytosis.

### *3.5 Soft CSCs enhance drug release and intracellular retention of N-GQD-delivered drugs*

According to the FRET principle illustrated in Fig. 1H, the emission ratio of N-GQD/Dox represents the relative drug release rate. The data show that CSCs had higher cellular uptake of N-GQD@Dox than bulk tumor cells (Fig. 5A-B, Fig. S10A-B). The fluorescence intensity of N-GQD and N-GQD/Dox ratio were time-dependent and significantly higher in CSCs than in bulk tumor cells (Fig. 5C-D, Fig. S10C-D), suggesting higher level of drug release in CSCs. The pH is known to influence drug release [37]. Soft CSCs had lower intracellular pH than stiff bulk tumor cells (Fig. S11A-C). Softening bulk tumor cells reduced the pH to the similar level of CSCs, while stiffening cells enhanced the intracellular pH. These findings suggest that soft CSCs may enhance drug release possibly through lowering down the intracellular pH.

Drug-resistant cancer cells and CSCs have the ability to expel out drugs [2]. To test this possibility, cellular retention of N-GQD@Dox and free Dox was examined after removing the extracellular nanoparticles and free Dox. Soft CSCs exhibited higher uptake of free Dox in the beginning but lower total and normalized amount later than stiff bulk tumor cells (Fig.

5E, F, and H, Fig. S10E, F, and H). In contrast, CSCs had significantly higher total and normalized amount of intracellular N-GQD@Dox than control cells (except at 16 h in Fig. 5G; Fig. 5G, I, Fig. S10G and I). The endocytosed free Dox and N-GQD@Dox were excreted gradually along with time (Fig. 5F-I, Fig. S10F-I), while N-GQDs were stably retained in both breast cancer cells and CSCs (Fig. S10J, K). These results suggest that soft CSCs enhance cellular retention of N-GQD@Dox, which may be ascribed to the suppression of CSC's excretion ability. To test this idea, we compared the expressions of exocytosis-related Rab GTPases Rab27a and Rab33b that promotes and suppresses exocytosis, respectively [38,39]. CSCs expressed higher Rab27a than bulk tumor cells (Fig. S11D, E). Free Dox up- and down-regulated Rab27a and Rab33b in both CSCs and bulk tumor cells, respectively, while CSCs exhibited higher Rab27a and lower Rab33b, which may explain the reduced cellular retention of free Dox in soft CSCs. In contrast, N-GQD@Dox increased and decreased the expression of Rab27a in bulk tumor cells and CSCs, respectively, but up-regulated Rab33b in both cells. The decrease/increase in pro-/anti-exocytosis genes may partially explain the enhanced cellular retention of N-GQD@Dox in soft CSCs.

### *3.6 Drug-loaded nanoparticles specifically eliminate soft CSCs and suppress tumor growth and xenograft tumorigenicity*

To test the potential of N-GQD@Dox in specific CSC targeting, the endocytosed nanoparticles need to be localized in the nucleus. N-GQD@Dox had higher levels of nuclear accumulation in CSCs than bulk tumor cells, while free Dox exhibited the opposite trend (Fig. S12). Therefore, the elevated cellular uptake, retention, drug release, and nuclear accumulation in CSCs may endow N-GQD@Dox with the ability to specifically eliminate these soft and malignant cancer cells. To test this idea, breast cancer cells and CSCs were treated with PBS, N-GQD, free Dox, and N-GQD@Dox, respectively. CSCs exhibited higher

cell viability than bulk tumor cells under free Dox (Fig. 6A), probably due to the higher drug excretion ability in CSCs. In contrast, breast CSCs had considerably lower viability than control cells in the presence of N-GQD@Dox. When the overall amount of Dox in N-GQD@Dox was equivalent to free Dox, cell viability was higher in N-GQD@Dox (Fig. 6A), which may be due to the partial drug release. We next tested the ability of N-GQD@Dox to specifically target CSCs in the whole breast cancer population. Compared to N-GQDs, free Dox increased the portion of breast CSCs CD133+ cells from 1.7% to 4.8% [1], while N-GQD@Dox decreased this portion to 0.9% (Fig. 6B-C), which may be due to the fact that CD133+ cells take up more N-GQD@Dox than CD133- cells (Fig. S13A). Further, free Dox enhanced tumor colony formation of the treated cells in soft agar, while N-GQD@Dox considerably suppressed this ability (Fig. 6D, Fig. S13B, C). In addition, the expressions of breast CSC markers Bmi-1 and CXCR4 were up-/down-regulated in the presence of free DOX and N-GQD@Dox (Fig. S13D-H). These results suggest that N-GQD@Dox has the ability to specifically eliminate while free Dox enriches soft CSCs *in vitro*.

Further, we examined the ability of N-GQD@Dox for specific CSC targeting in breast tumor xenografts. The biodistribution shows that free Dox had high accumulation in the heart, spleen, liver, lung, and kidney, while N-GQD@Dox was more localized in the tumor tissues (Fig. 6H), suggest that N-GQD@Dox may target cancer with minimum side effects. Both free Dox and N-GQD@Dox significantly suppressed tumor growth and reduced tumor weight to the similar extent compared to N-GQDs (Fig. 6E-F, Fig. S14A). Remarkably, N-GQD@Dox considerably reduced the CD133+ subpopulation in the treated tumors from 3.3% to 2.3% compared to N-GQD, while free Dox increased this fraction to ~9.0% (Fig. 6G, Fig. S14B). The CSC marker Bmi-1 was enhanced in tumor xenografts treated with free Dox but suppressed in the tumors treated with N-GQD@Dox (Fig. S14D). Importantly, N-

GQD@Dox had no obvious side effect on the body weight of the treated mice, while free Dox considerably suppressed animal growth (Fig. 6I). Further, N-GQD@Dox-treated xenograft cells generated smaller tumors than N-GQD, while Dox-treated tumor cells formed larger xenografts (Fig. 6J), suggesting that N-GQD@Dox suppresses the tumorigenicity of xenograft cells. There was no significant difference in animal body weight among different conditions (Fig. S14C). All these findings suggest that drug-loaded N-GQDs specifically eliminate soft CSCs and suppress tumor growth and xenograft tumorigenicity without obvious side effects on animal growth.

### *3.7 Discussion*

As an essential step in drug delivery, the entry of nanoparticles into cancer cells depends on the mechanics of both the microenvironment and nanoparticles [13,40]. Stiff substrates increase cell spreading and contractility that dictate low uptake of nanoparticles [41,42]. Low rigidity of microparticles enhances their endocytosis and drug delivery efficiency [43]. Compared to stiff ones, soft nanolipogels exhibit tumor accumulation and preferential internalization by tumor cells [44], while soft polyethylene glycol-based nanoparticles show increased circulation time and lung targeting but reduced cellular uptake in cancer cells [45]. Although the mechanics of tumor cells have been intensively investigated and correlate with cancer malignancy and stemness, their roles in nanoparticle uptake and cancer targeting remain unknown. This study has demonstrated that soft CSCs take up more nanoparticles per unit area than stiff bulk tumor cells. Softening bulk tumor cells significantly increases cellular uptake, while stiffening bulk tumor cells and CSCs considerably suppresses nanoparticle endocytosis. These findings together with many others suggest that the softness (the inverse of stiffness) of not only substrate and nanoparticle but also cancer cells enhances cellular uptake. Interestingly, moderately softening both bulk tumor cells (up to 6 μM

Blebbistatin) and CSCs (up to 2 μM Blebbistatin) enhances cellular uptake, while considerably softening them (20 μM Blebbistatin) suppresses nanoparticle internalization. This finding suggests that certain levels of cytoskeleton and myosin activity may be required for N-GQD uptake, which is supported by previous reports that cytoskeleton is involved in the entry of nanoparticles into living cells [3,27,46]. Note that the treatment by 6 μM Blebbistatin facilitates cellular uptake in bulk tumor cells while shows no effect on soft CSCs, which might be due to two possibilities. One is that CSCs already exhibit relatively weaker cytoskeleton and lower stiffness than bulk tumor cells. Another possibility may be that in addition to low cellular stiffness, CSCs hold several other unique properties, including high stemness, which may also contribute to the characteristic behavior in nanoparticle uptake.

We further show that cell mechanics regulate nanoparticle uptake partially through the effect on caveolae-/clathrin-dependent endocytosis pathways, consistent with the previous finding that cellular contractility suppresses nanoparticle endocytosis per unit area [41,42]. However, it is still not clear how cell mechanics influence the caveolae-/clathrin-dependent endocytosis. Note that inhibiting both caveolae-/clathrin-dependent endocytosis only decreases the internalization by ~40%, suggesting that these endocytosis pathways partially contribute to nanoparticle uptake. This may be due to several reasons. First, low doses of the drugs that inhibit clathrin and caveolae-mediated endocytosis are utilized in this study, since high doses are cytotoxic to tumor cells. Second, in addition to these endocytosis pathways, nanoparticle uptake could be mediated by other mechanisms [3,47], such as clathrin-independent but dynamin-dependent pathway, clathrin and dynamin-independent endocytosis, macropinocytosis, and phagocytosis. Third, the size of quantum dots is about 3 nm, comparable with the membrane bilayer dimension. It is possible that the spontaneous

transmembrane penetration cooperates with various endocytosis mechanisms in the N-GQD internalization [48].

This study demonstrates that drug-loaded N-GQDs are preferentially internalized by soft CSCs with enhanced drug release, cellular retention, and nuclear accumulation compared to stiff bulk tumor cells. This nanocarrier-drug complex specifically eliminates CSC fraction both *in vitro* and *in vivo* and suppresses the growth and tumorigenicity of tumor xenografts but not animal body growth. In contrast, free Dox markedly enriches CSCs within the tumor, suppresses body growth, and promotes the tumorigenicity of xenograft cells. These results suggest that low cellular stiffness is required for efficient nanoparticle uptake in malignant CSCs and can be harnessed for the specific elimination of CSCs within the heterogeneous tumor with minimum side effect. Drug-loaded N-GQDs can specifically target soft CSCs, suppress primary tumor growth, and probably reduce the risk of tumor recurrence and metastasis, which needs to be examined in the future. In addition to low cell stiffness, it is possible that other unique properties of CSCs are also involved in the enhanced nanoparticle uptake, cellular retention, drug release, and nuclear accumulation, and eventually in CSC targeting. Therefore, drug-loaded N-GQDs preferentially eradicate soft CSCs partially by targeting their low cellular stiffness and suppress tumor growth. Nevertheless, although low stiffness of CSCs is not limited to breast cancer, whether the nanoparticle-based mechanomedicine can specifically eliminate soft CSCs in other types of cancer still requires rigorous investigation. Moreover, it remains unclear whether the role of cell mechanics in cellular uptake, retention, and nuclear accumulation is GQD-specific or can be further extended to other types of nanoparticles. Interestingly, free Dox enriches CSCs both *in vitro* and *in vivo*, consistent with the previous studies that chemotherapy drug paclitaxel greatly increases the CSC frequency by >10 fold in the patient-derived xenografts and enhances the

tumor sphere formation ability of drug-treated xenograft cells by 2-3 fold [49]. It is well known that CSCs are resistant to chemotherapy and contribute to chemoresistance and cancer relapse [50–54]. This study demonstrates a new strategy that cell softness can be harnessed as a unique biophysical feature for CSC eradication and the prevention of chemoresistance.

Anti-cancer drugs become effective after the release from the carrier. Cancer cells have lower extracellular pH (pHe: 6.7-7.1) and higher intracellular pH (pHi: ~7.6) than normal cells (pHe: ~7.4; pHi: ~7.2) [55]. The extracellular acidosis and intracellular alkalization suppress drug release and thus reduce the efficacy. We show that soft CSCs have lower intracellular pH than stiff bulk tumor cells and softening/stiffening cells decreases/increases cellular pH. The reduction in the intracellular pH may facilitate the disruption of the π-π interaction between drugs and N-GQDs and thus enhance the release rate [32]. It remains unclear how the mechanics of soft CSCs induce low intracellular pH. After cellular uptake and drug release, some cancer cells have the ability to excrete the internalized drugs [56]. Soft CSCs exhibit high cellular uptake and retention of N-GQD@Dox but not free Dox, which may be due to the reduced exocytosis. Note that both soft CSCs and bulk tumor cells stably retain the endocytosed N-GQDs, suggesting that N-GQD alone may overcome tumor cell excretion. In comparison, free Dox affects exocytosis in the opposite manner. These findings suggest that N-GQD@Dox has inhibitory effect on the excretion of delivered drugs in soft CSCs.

## 4. Conclusion

This study has demonstrated that cell mechanics regulate N-GQD uptake partially through the effect on caveolae-/clathrin-dependent endocytosis. Low cellular stiffness enhances drug release, nuclear localization, and cellular retention of drug-loaded N-GQDs in CSCs possibly due to the decrease in intracellular pH and the repression of exocytosis. Compared to free

drugs, drug-loaded N-GQDs specifically eliminate soft CSCs both *in vitro* and *in vivo* and suppress tumor growth with minimum side effect. These findings demonstrate the regulatory role and therapeutic significance of cell mechanics in nanoparticle-mediated specific CSC targeting.

**Declaration of Competing Interest**

The authors declare no competing financial interest.

**Acknowledgements**

We thank Sanjay Kumar (University of California, Berkeley) for the kind gifts of pSLIK CA-MLCK, pSLIK CA-ROCK, and pSLIK-Venus (empty) plasmids, Tai Chi-shing William (Hong Kong Polytechnic University) for the plasmid preparation, the University Life Science Facility in the Hong Kong Polytechnic University for providing flow cytometry equipment and confocal laser scanning microscopy, and the Hong Kong Polytechnic University Shenzhen Research Institute for providing the central animal facility. We acknowledge the support from National Natural Science Foundation of China (Project no. 11972316 and 31771077), Shenzhen Science and Technology Innovation Commission (Project no. JCYJ20170413154735522, JCYJ20200109142001798, and SGDX2020110309520303), Early Career Scheme from Research Grants Council of the Hong Kong Special Administrative Region, China (PolyU 252094/17E), Collaborative Research Grant of Hong Kong Research Grant Council (C5011-19G), General Research Fund of Hong Kong Research Grant Council (PolyU 15216917 and 15214619), and the internal grant from the Hong Kong Polytechnic University (1-ZVPD, 1-BBB1, and 1-ZE1E).

**Supplementary materials**

The Supplementary material includes 14 supplementary figures, 1 video, and 1 table.

**References**


[1] L. V Nguyen, R. Vanner, P. Dirks, C.J. Eaves, Cancer stem cells: an evolving concept., Nat. Rev. Cancer. 12 (2012) 133–43.

[2] M. Dean, T. Fojo, S. Bates, Tumour stem cells and drug resistance., Nat. Rev. Cancer. 5 (2005) 275–84.

[3] S. Behzadi, V. Serpooshan, W. Tao, M.A. Hamaly, M.Y. Alkawareek, E.C. Dreaden, D. Brown, A.M. Alkilany, O.C. Farokhzad, M. Mahmoudi, Cellular uptake of nanoparticles: journey inside the cell, Chem. Soc. Rev. 46 (2017) 4218–4244.

[4] J. Kim, A. Dey, A. Malhotra, J. Liu, S.I. Ahn, Y.J. Sei, A.M. Kenney, T.J. MacDonald, Y.T. Kim, Engineered biomimetic nanoparticle for dual targeting of the cancer stem-like cell population in sonic hedgehog medulloblastoma, Proc. Natl. Acad. Sci. U. S. A. 117 (2020) 24205–24212.

[5] D. Liu, Y. Hong, Y. Li, C. Hu, T.C. Yip, W.K. Yu, Y. Zhu, C.C. Fong, W. Wang, S.K. Au, S. Wang, M. Yang, Targeted destruction of cancer stem cells using multifunctional magnetic nanoparticles that enable combined hyperthermia and chemotherapy, Theranostics. 10 (2020) 1181–1196.

[6] E. Quintana, M. Shackleton, M.S. Sabel, D.R. Fullen, T.M. Johnson, S.J. Morrison, Efficient tumour formation by single human melanoma cells., Nature. 456 (2008) 593–8.

[7] P.B. Gupta, C.L. Chaffer, R.A. Weinberg, Cancer stem cells: mirage or reality?, Nat. Med. 15 (2009) 1010–1012.

[8] T.S. Hauck, A.A. Ghazani, W.C.W. Chan, Assessing the Effect of Surface Chemistry

on Gold Nanorod Uptake, Toxicity, and Gene Expression in Mammalian Cells, Small. 4 (2008) 153–159.

[9] E.C. Cho, J. Xie, P.A. Wurm, Y. Xia, Understanding the Role of Surface Charges in Cellular Adsorption versus Internalization by Selectively Removing Gold Nanoparticles on the Cell Surface with a $I_2$ /KI Etchant, Nano Lett. 9 (2009) 1080–1084.

[10] W. Jiang, B.Y.S. Kim, J.T. Rutka, W.C.W. Chan, Nanoparticle-mediated cellular response is size-dependent, Nat. Nanotechnol. 3 (2008) 145–150.

[11] S.E.A. Gratton, P.A. Ropp, P.D. Pohlhaus, J.C. Luft, V.J. Madden, M.E. Napier, J.M. DeSimone, The effect of particle design on cellular internalization pathways., Proc. Natl. Acad. Sci. U. S. A. 105 (2008) 11613–8.

[12] S. Zhang, J. Li, G. Lykotrafitis, G. Bao, S. Suresh, Size-Dependent Endocytosis of Nanoparticles, Adv. Mater. 21 (2009) 419–424.

[13] D. Wirtz, K. Konstantopoulos, P.C. Searson, The physics of cancer: the role of physical interactions and mechanical forces in metastasis., Nat. Rev. Cancer. 11 (2011) 512–22.

[14] N. Wang, J.D. Tytell, D.E. Ingber, Mechanotransduction at a distance: mechanically coupling the extracellular matrix with the nucleus., Nat. Rev. Mol. Cell Biol. 10 (2009) 75–82.

[15] S. Suresh, Biomechanics and biophysics of cancer cells, Acta Biomater. 3 (2007) 413–438.

[16] S.E. Cross, Y.-S. Jin, J. Rao, J.K. Gimzewski, Nanomechanical analysis of cells from cancer patients., Nat. Nanotechnol. 2 (2007) 780–3.

[17] V. Swaminathan, K. Mythreye, E.T. O'Brien, A. Berchuck, G.C. Blobe, R. Superfine, Mechanical stiffness grades metastatic potential in patient tumor cells and in cancer cell lines., Cancer Res. 71 (2011) 5075–80.

[18] J. Liu, Y. Tan, H. Zhang, Y. Zhang, P. Xu, J. Chen, Y.-C. Poh, K. Tang, N. Wang, B. Huang, Soft fibrin gels promote selection and growth of tumorigenic cells., Nat. Mater. 11 (2012) 734–41.

[19] W. Zhang, K. Kai, D.S. Choi, T. Iwamoto, Y.H. Nguyen, H. Wong, M.D. Landis, N.T. Ueno, J. Chang, L. Qin, Microfluidics separation reveals the stem-cell-like deformability of tumor-initiating cells., Proc. Natl. Acad. Sci. U. S. A. 109 (2012) 18707–12.

[20] J. Ma, Y. Zhang, K. Tang, H. Zhang, X. Yin, Y. Li, P. Xu, Y. Sun, R. Ma, T. Ji, J. Chen, S. Zhang, T. Zhang, S. Luo, Y. Jin, X. Luo, C. Li, H. Gong, Z. Long, J. Lu, Z. Hu, X. Cao, N. Wang, X. Yang, B. Huang, Reversing drug resistance of soft tumor-repopulating cells by tumor cell-derived chemotherapeutic microparticles, Cell Res. 26 (2016) 713–727.

[21] J. Lv, Y. Liu, F. Cheng, J. Li, Y. Zhou, T. Zhang, N. Zhou, C. Li, Z. Wang, L. Ma, M. Liu, Q. Zhu, X. Liu, K. Tang, J. Ma, H. Zhang, J. Xie, Y. Fang, H. Zhang, N. Wang, Y. Liu, B. Huang, Cell softness regulates tumorigenicity and stemness of cancer cells, EMBO J. 40 (2021) e106123.

[22] Y. Qin, K. Chen, W. Gu, X. Dong, R. Lei, Y. Chang, X. Bai, S. Xia, L. Zeng, J. Zhang, S. Ma, J. Li, S. Li, G. Xing, Small size fullerenol nanoparticles suppress lung metastasis of breast cancer cell by disrupting actin dynamics, J. Nanobiotechnology. 16 (2018) 54.

[23] W. Xu, R. Mezencev, B. Kim, L. Wang, J. McDonald, T. Sulchek, Cell stiffness is a

biomarker of the metastatic potential of ovarian cancer cells., PLoS One. 7 (2012) e46609.

[24] Y. Liu, T. Zhang, H. Zhang, J. Li, N. Zhou, R. Fiskesund, J. Chen, J. Lv, J. Ma, H. Zhang, K. Tang, F. Cheng, Y. Zhou, X. Zhang, N. Wang, B. Huang, Cell Softness Prevents Cytolytic T-cell Killing of Tumor-Repopulating Cells, Cancer Res. 81 (2021) 476–488.

[25] Y. Xin, X. Chen, X. Tang, K. Li, M. Yang, W.C.-S. Tai, Y. Liu, Y. Tan, Mechanics and Actomyosin-Dependent Survival/Chemoresistance of Suspended Tumor Cells in Shear Flow, Biophys. J. 116 (2019) 1803–1814.

[26] J. Chen, W. Zhou, Q. Jia, J. Chen, S. Zhang, W. Yao, F. Wei, Y. Zhang, F. Yang, W. Huang, Y. Zhang, H. Zhang, Y. Zhang, B. Huang, Z. Zhang, H. Jia, N. Wang, Efficient extravasation of tumor-repopulating cells depends on cell deformability., Sci. Rep. 6 (2016) 19304.

[27] M. Sousa De Almeida, E. Susnik, B. Drasler, P. Taladriz-Blanco, A. Petri-Fink, B. Rothen-Rutishauser, Understanding nanoparticle endocytosis to improve targeting strategies in nanomedicine, Chem. Soc. Rev. 50 (2021) 5397–5434.

[28] B.D. Chithrani, A. Arezou A. Ghazani,, W.C.W. Chan, Determining the Size and Shape Dependence of Gold Nanoparticle Uptake into Mammalian Cells, Nano Lett. 6 (2006) 662–668.

[29] B.D.C. And, W.C.W. Chan, Elucidating the Mechanism of Cellular Uptake and Removal of Protein-Coated Gold Nanoparticles of Different Sizes and Shapes, Nano Lett. 7 (2007) 1542–1550.

[30] J. Mosquera, I. García, L.M. Liz-Marzán, Cellular Uptake of Nanoparticles versus Small Molecules: A Matter of Size, Acc. Chem. Res. 51 (2018) 2305–2313.

[31] Y. Yan, J. Gong, J. Chen, Z. Zeng, W. Huang, K. Pu, J. Liu, P. Chen, Recent Advances on Graphene Quantum Dots: From Chemistry and Physics to Applications, Adv. Mater. 31 (2019) 1808283.

[32] X. Su, C. Chan, J. Shi, M.-K. Tsang, Y. Pan, C. Cheng, O. Gerile, M. Yang, A graphene quantum dot@Fe3O4@SiO2 based nanoprobe for drug delivery sensing and dual-modal fluorescence and MRI imaging in cancer cells, Biosens. Bioelectron. 92 (2017) 489–495.

[33] J. Jin, K. Tang, Y. Xin, T. Zhang, Y. Tan, Hemodynamic shear flow regulates biophysical characteristics and functions of circulating breast tumor cells reminiscent of brain metastasis, Soft Matter. 14 (2018) 9528–9533.

[34] Y. Tan, A. Tajik, J.J.J. Chen, Q. Jia, F. Chowdhury, L. Wang, J.J.J. Chen, S. Zhang, Y. Hong, H. Yi, D.C.D.C. Wu, Y. Zhang, F. Wei, Y.-C.Y.-C. Poh, J. Seong, R. Singh, L.-J. Lin, S. Doğanay, Y. Li, H. Jia, T. Ha, Y. Wang, B.B. Huang, N. Wang, S. Doğanay, Y. Li, H. Jia, T. Ha, Y. Wang, B.B. Huang, N. Wang, Matrix softness regulates plasticity of tumour-repopulating cells via H3K9 demethylation and Sox2 expression, Nat. Commun. 5 (2014) 4619.

[35] W. Anderson, D. Kozak, V.A. Coleman, Å.K. Jämting, M. Trau, A comparative study of submicron particle sizing platforms: Accuracy, precision and resolution analysis of polydisperse particle size distributions, J. Colloid Interface Sci. 405 (2013) 322–330.

[36] M.J. Paszek, N. Zahir, K.R. Johnson, J.N. Lakins, G.I. Rozenberg, A. Gefen, C.A. Reinhart-King, S.S. Margulies, M. Dembo, D. Boettiger, D.A. Hammer, V.M. Weaver, Tensional homeostasis and the malignant phenotype., Cancer Cell. 8 (2005) 241–54.

[37] W. Gao, J.M. Chan, O.C. Farokhzad, pH-Responsive Nanoparticles for Drug Delivery, Mol. Pharm. 7 (2010) 1913–1920.

[38] S. Zografou, D. Basagiannis, A. Papafotika, R. Shirakawa, H. Horiuchi, D. Auerbach, M. Fukuda, S. Christoforidis, A complete Rab screening reveals novel insights in Weibel-Palade body exocytosis., J. Cell Sci. 125 (2012) 4780–90.

[39] H. Stenmark, Rab GTPases as coordinators of vesicle traffic, Nat. Rev. Mol. Cell Biol. 10 (2009) 513–525.

[40] S. Kumar, V.M. Weaver, Mechanics, malignancy, and metastasis: the force journey of a tumor cell., Cancer Metastasis Rev. 28 (2009) 113–27.

[41] Q. Wei, C. Huang, Y. Zhang, T. Zhao, P. Zhao, P. Butler, S. Zhang, Mechanotargeting: Mechanics-Dependent Cellular Uptake of Nanoparticles, Adv. Mater. 30 (2018) 1707464.

[42] C. Huang, P.J. Butler, S. Tong, H.S. Muddana, G. Bao, S. Zhang, Substrate Stiffness Regulates Cellular Uptake of Nanoparticles, Nano Lett. 13 (2013) 1611–1615.

[43] Q. Liang, N. Bie, T. Yong, K. Tang, X. Shi, Z. Wei, H. Jia, X. Zhang, H. Zhao, W. Huang, L. Gan, B. Huang, X. Yang, The softness of tumour-cell-derived microparticles regulates their drug-delivery efficiency, Nat. Biomed. Eng. 3 (2019) 729–740.

[44] P. Guo, D. Liu, K. Subramanyam, B. Wang, J. Yang, J. Huang, D.T. Auguste, M.A. Moses, Nanoparticle elasticity directs tumor uptake, Nat. Commun. 9 (2018) 130.

[45] A.C. Anselmo, M. Zhang, S. Kumar, D.R. Vogus, S. Menegatti, M.E. Helgeson, S. Mitragotri, Elasticity of Nanoparticles Influences Their Blood Circulation, Phagocytosis, Endocytosis, and Targeting, ACS Nano. 9 (2015) 3169–3177.

[46] L.W. Zhang, N.A. Monteiro-Riviere, Mechanisms of quantum dot nanoparticle cellular uptake, Toxicol. Sci. 110 (2009) 138–155.

[47] J.J. Rennick, A.P.R. Johnston, R.G. Parton, Key principles and methods for studying the endocytosis of biological and nanoparticle therapeutics, Nat. Nanotechnol. 16 (2021) 266–276.

[48] Y. Roiter, M. Ornatska, A.R. Rammohan, J. Balakrishnan, D.R. Heine, S. Minko, Interaction of nanoparticles with lipid membrane, Nano Lett. 8 (2008) 941–944.

[49] S. Zhang, H. Zhang, E.M. Ghia, J. Huang, L. Wu, J. Zhang, S. Lam, Y. Lei, J. He, B. Cui, G.F. Widhopf, J. Yu, R. Schwab, K. Messer, W. Jiang, B.A. Parker, D.A. Carson, T.J. Kipps, Inhibition of chemotherapy resistant breast cancer stem cells by a ROR1 specific antibody, Proc. Natl. Acad. Sci. U. S. A. 116 (2019) 1370–1377.

[50] J. Chen, Y. Li, T.-S. Yu, R.M. McKay, D.K. Burns, S.G. Kernie, L.F. Parada, A restricted cell population propagates glioblastoma growth after chemotherapy., Nature. 488 (2012) 522–6.

[51] B.B. Liau, C. Sievers, L.K. Donohue, S.M. Gillespie, W.A. Flavahan, T.E. Miller, A.S. Venteicher, C.H. Hebert, C.D. Carey, S.J. Rodig, S.J. Shareef, F.J. Najm, P. van Galen, H. Wakimoto, D.P. Cahill, J.N. Rich, J.C. Aster, M.L. Suvà, A.P. Patel, B.E. Bernstein, Adaptive Chromatin Remodeling Drives Glioblastoma Stem Cell Plasticity and Drug Tolerance, Cell Stem Cell. 20 (2017) 233–246.

[52] A. Sánchez-Danés, J.C. Larsimont, M. Liagre, E. Muñoz-Couselo, G. Lapouge, A. Brisebarre, C. Dubois, M. Suppa, V. Sukumaran, V. Del Marmol, J. Tabernero, C. Blanpain, A slow-cycling LGR5 tumour population mediates basal cell carcinoma relapse after therapy, Nature. 562 (2018) 434–438.

[53] D. Shiokawa, H. Sakai, H. Ohata, T. Miyazaki, Y. Kanda, S. Sekine, D. Narushima, M. Hosokawa, M. Kato, Y. Suzuki, H. Takeyama, H. Kambara, H. Nakagama, K. Okamoto, Slow-cycling cancer stem cells regulate progression and chemoresistance in

colon cancer, Cancer Res. 80 (2021) 4451–4464.

[54] S. Boumahdi, F.J. de Sauvage, The great escape: tumour cell plasticity in resistance to targeted therapy, Nat. Rev. Drug Discov. 19 (2020) 39–56.

[55] T. Henning, M. Kraus, M. Brischwein, A.M. Otto, B. Wolf, Relevance of tumor microenvironment for progression, therapy and drug development., Anticancer. Drugs. 15 (2004) 7–14.

[56] T. Yong, X. Zhang, N. Bie, H. Zhang, X. Zhang, F. Li, A. Hakeem, J. Hu, L. Gan, H.A. Santos, X. Yang, Tumor exosome-based nanoparticles are efficient drug carriers for chemotherapy, Nat. Commun. 10 (2019) 3838.

## Figures

## Fig. 1

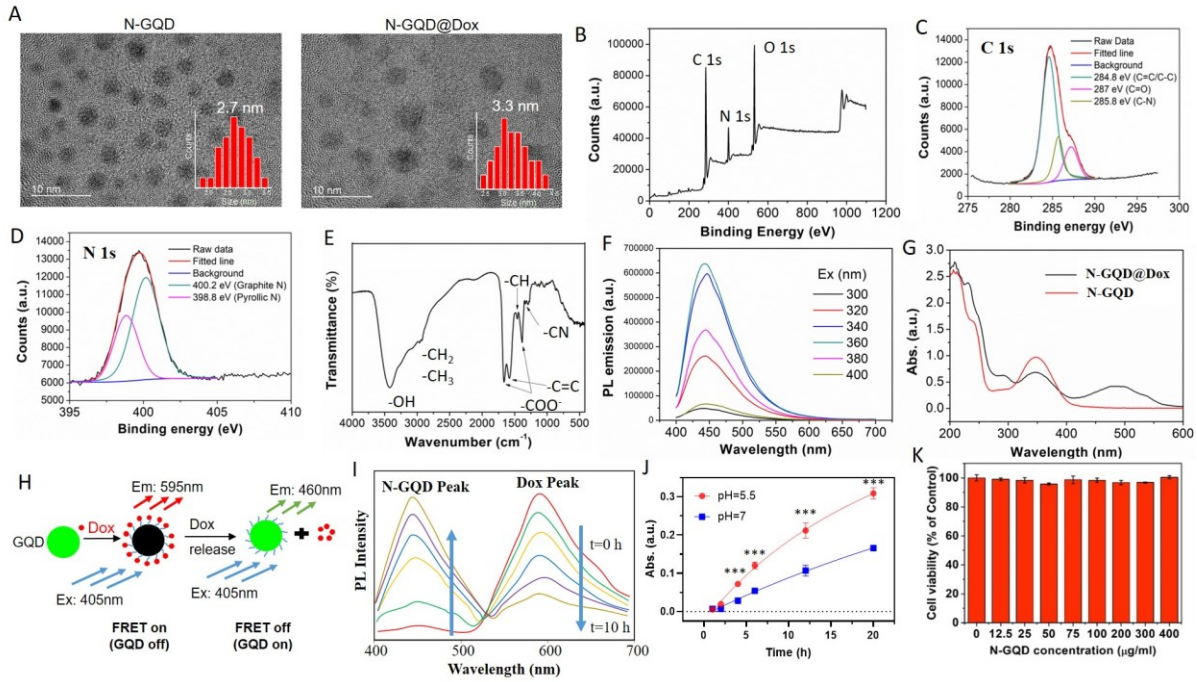

**Fig. 2**

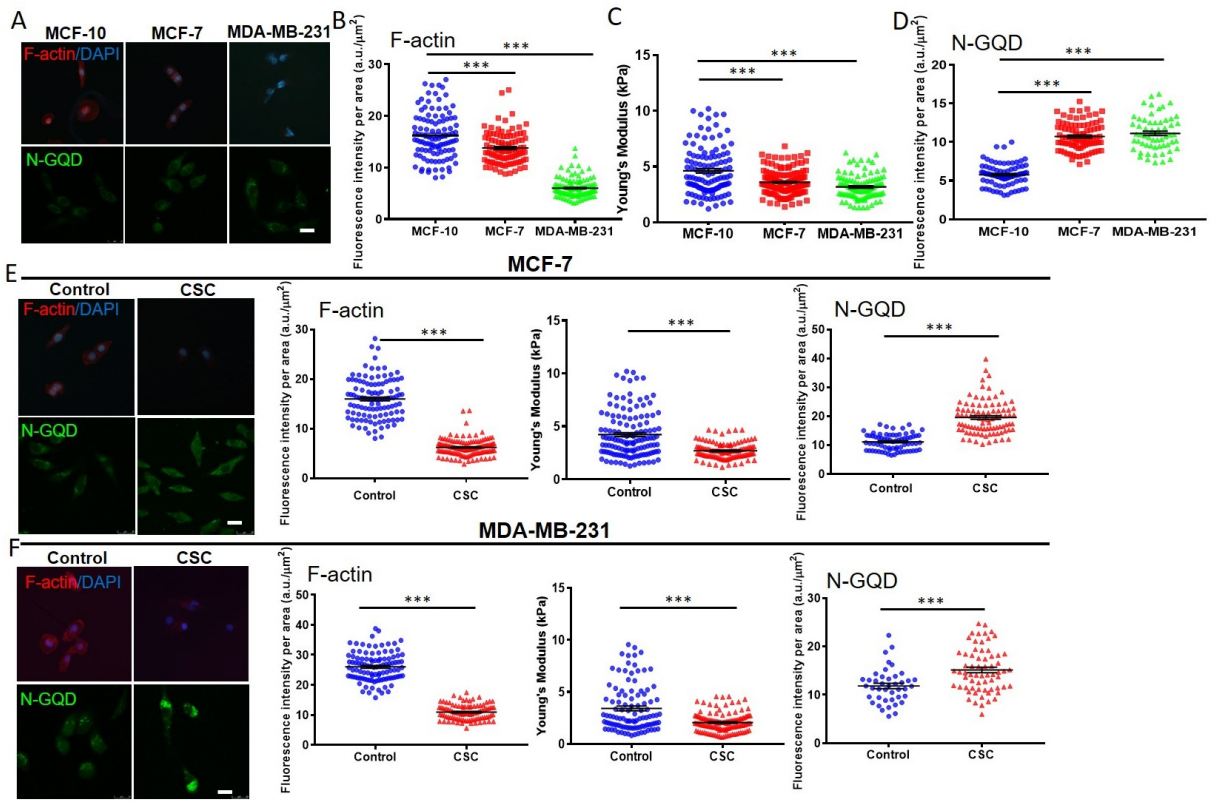
A
MCF-10
MCF-7
MDA-MB-231
F-actin/DAPI
N-GQD
B
F-actin
Fluorescence intensity per area (a.u./μm²)
MCF-10
MCF-7
MDA-MB-231
C
Young's Modulus (kPa)
D
N-GQD
E
MCF-7
Control
CSC
F
MDA-MB-231
***

**Fig. 3**

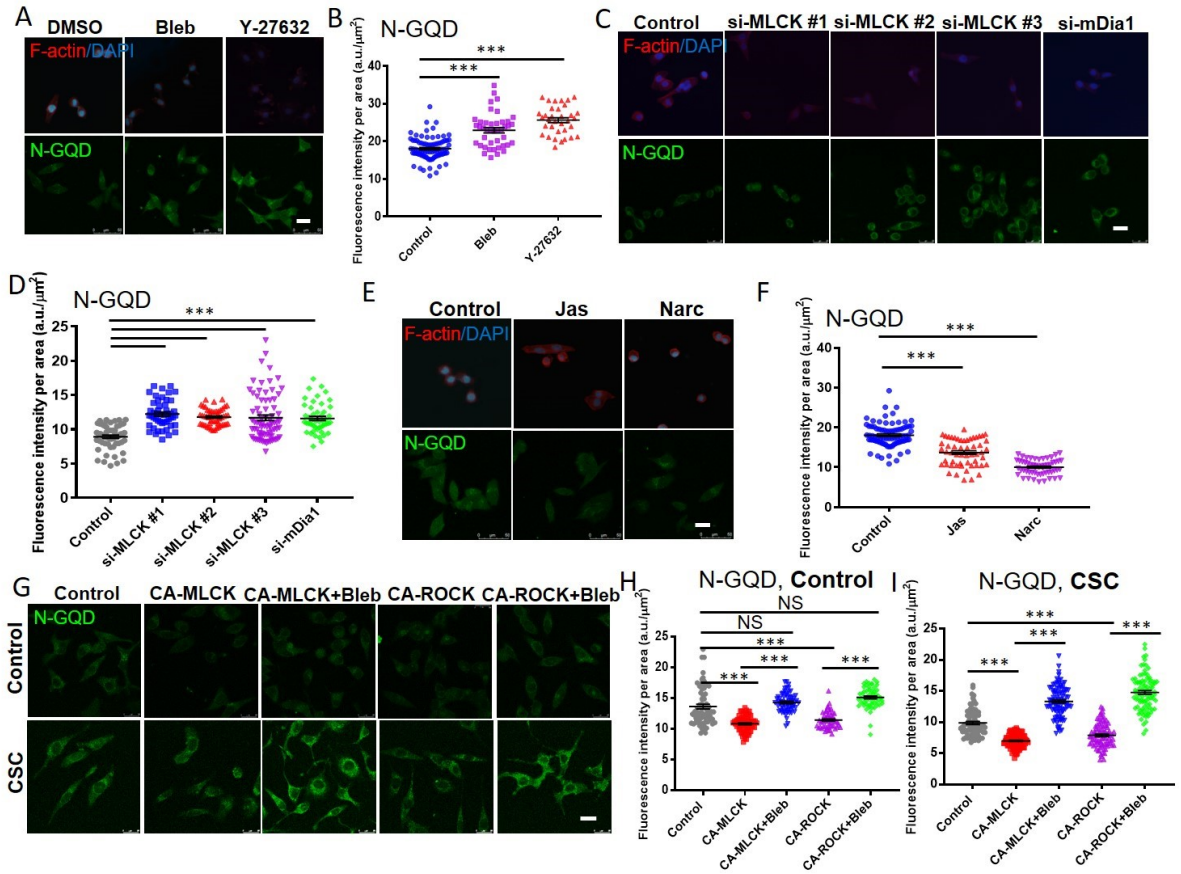
A
DMSO
Bleb
Y-27632
F-actin/DAPI
N-GQD
B
N-GQD
***
***
Fluorescence intensity per area (a.u./μm²)
Control
Bleb
Y-27632
C
Control
si-MLCK #1
si-MLCK #2
si-MLCK #3
si-mDia1
F-actin/DAPI
N-GQD
D
N-GQD
***
Fluorescence intensity per area (a.u./μm²)
Control
si-MLCK #1
si-MLCK #2
si-MLCK #3
si-mDia1
E
Control
Jas
Narc
F-actin/DAPI
N-GQD
F
N-GQD
***
***
Fluorescence intensity per area (a.u./μm²)
Control
Jas
Narc
G
Control
CA-MLCK
CA-MLCK+Bleb
CA-ROCK
CA-ROCK+Bleb
N-GQD
Control
CSC
H
N-GQD, Control
NS
NS
***
***
***
***
Fluorescence intensity per area (a.u./μm²)
Control
CA-MLCK
CA-MLCK+Bleb
CA-ROCK
CA-ROCK+Bleb
I
N-GQD, CSC
***
***
***
***
Fluorescence intensity per area (a.u./μm²)
Control
CA-MLCK
CA-MLCK+Bleb
CA-ROCK
CA-ROCK+Bleb

**Fig. 4**

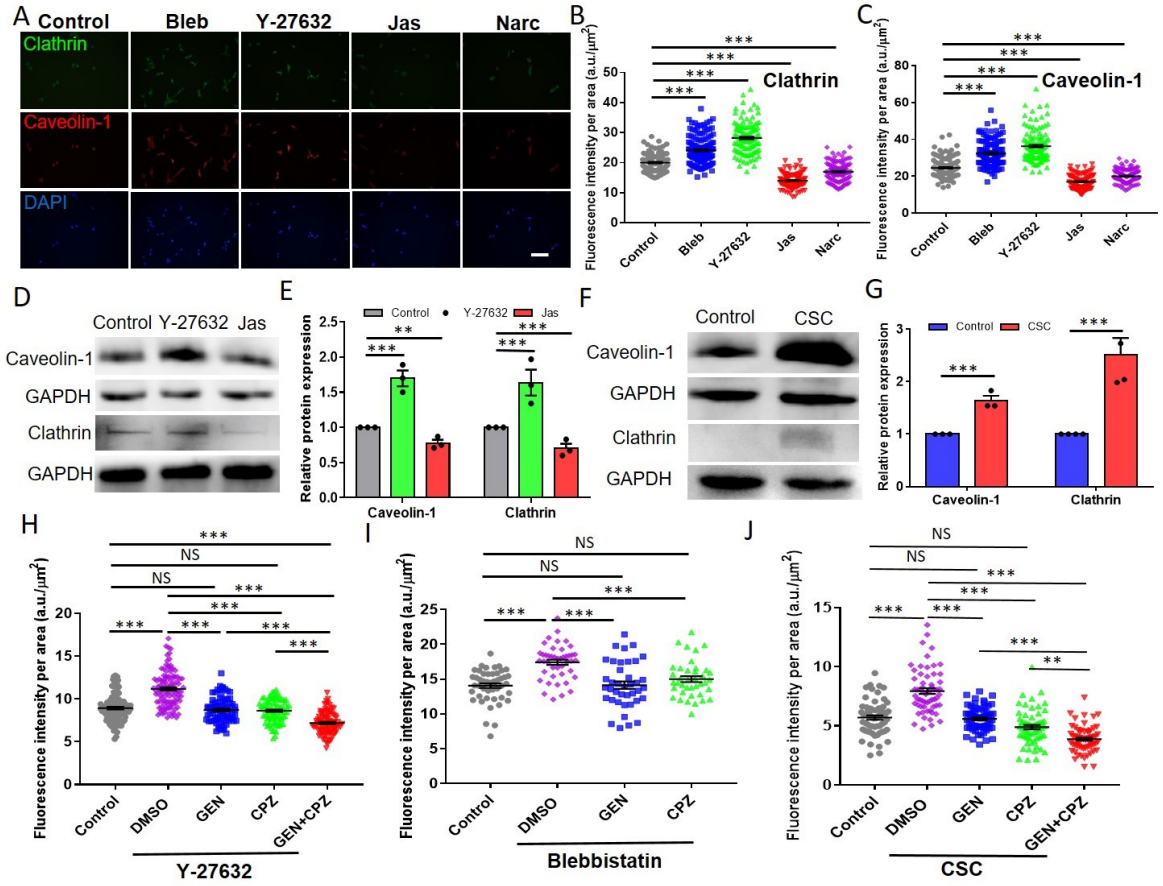
A
Control
Bleb
Y-27632
Jas
Narc
Clathrin
Caveolin-1
DAPI
B
Clathrin
Fluorescence intensity per area (a.u./μm²)
C
Caveolin-1
D
Control Y-27632 Jas
Caveolin-1
GAPDH
Clathrin
GAPDH
E
Control
Y-27632
Jas
Relative protein expression
Caveolin-1
Clathrin
F
Control
CSC
Caveolin-1
GAPDH
Clathrin
GAPDH
G
Control
CSC
Relative protein expression
Caveolin-1
Clathrin
H
Control
DMSO
GEN
CPZ
GEN+CPZ
Y-27632
I
Blebbistatin
J
CSC
NS
***
**

**Fig. 5**

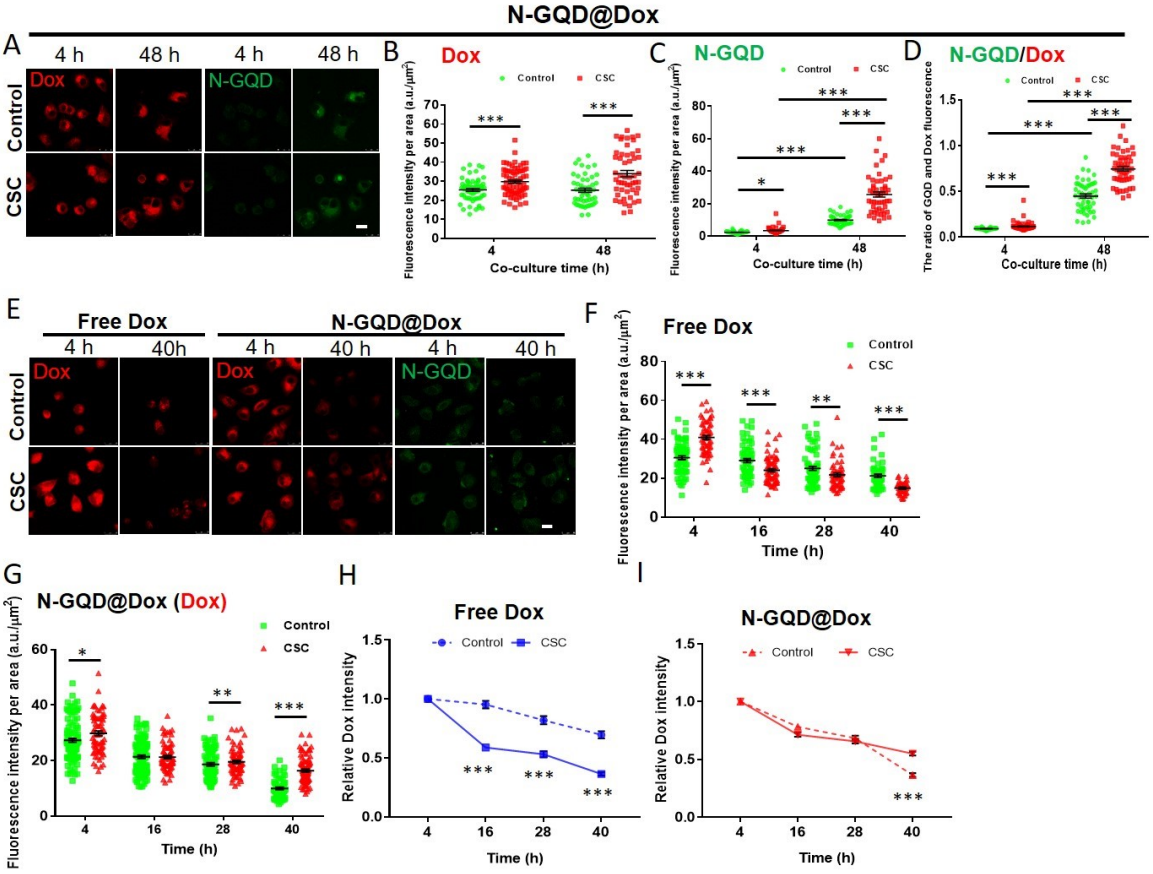
N-GQD@Dox
A
4 h
48 h
4 h
48 h
Dox
N-GQD
Control
CSC
B
Dox
C
N-GQD
D
N-GQD/Dox
Control
CSC
Fluorescence intensity per area (a.u./μm²)
The ratio of GQD and Dox fluorescence
Co-culture time (h)
E
Free Dox
N-GQD@Dox
4 h
40h
40 h
F
Free Dox
Time (h)
G
N-GQD@Dox (Dox)
H
Free Dox
Relative Dox intensity
I
N-GQD@Dox

**Fig. 6**

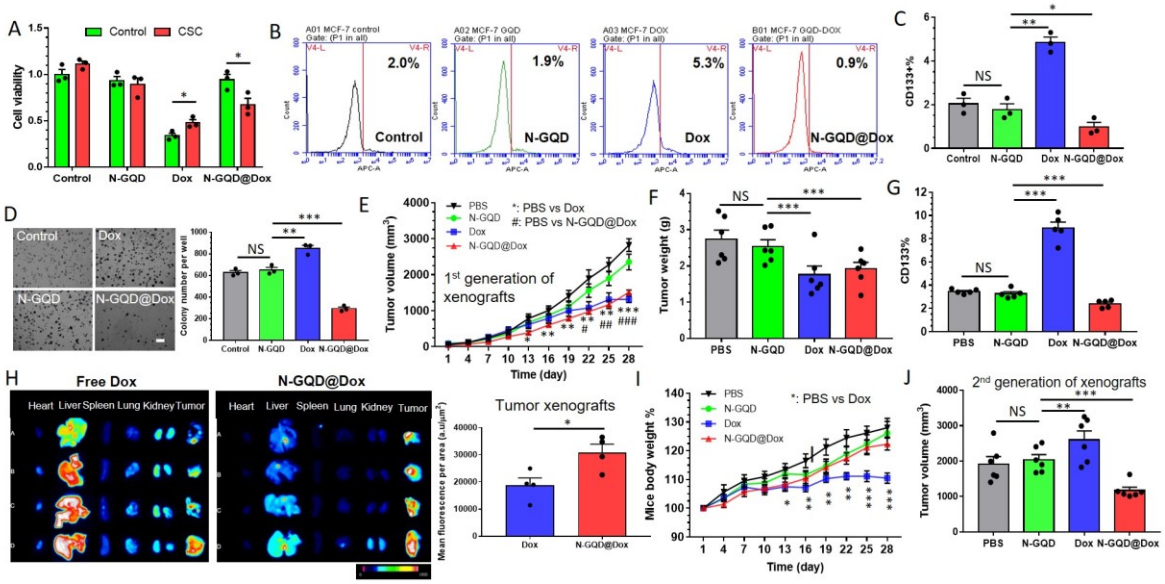
A
Control
CSC
Cell viability
Control
N-GQD
Dox
N-GQD@Dox
B
A01 MCF-7 control
A02 MCF-7 GQD
A03 MCF-7 DOX
B01 MCF-7 GQD-DOX
2.0%
1.9%
5.3%
0.9%
Control
N-GQD
Dox
N-GQD@Dox
C
CD133+%
NS
Control
N-GQD
Dox
N-GQD@Dox
D
Control
Dox
N-GQD
N-GQD@Dox
Colony number per well
NS
E
PBS
N-GQD
Dox
N-GQD@Dox
*: PBS vs Dox
#: PBS vs N-GQD@Dox
1st generation of xenografts
Tumor volume (mm3)
Time (day)
F
Tumor weight (g)
NS
PBS
N-GQD
Dox
N-GQD@Dox
G
CD133%
NS
PBS
N-GQD
Dox
N-GQD@Dox
H
Free Dox
N-GQD@Dox
Heart
Liver
Spleen
Lung
Kidney
Tumor
Tumor xenografts
Mean fluorescence per area (a.u/μm2)
Dox
N-GQD@Dox
I
PBS
N-GQD
Dox
N-GQD@Dox
*: PBS vs Dox
Mice body weight %
Time (day)
J
2nd generation of xenografts
NS
Tumor volume (mm3)
PBS
N-GQD
Dox
N-GQD@Dox